



Mass spectrometry-based phospholipid imaging: methods and findings

メタデータ	言語: English 出版者: 公開日: 2022-02-08 キーワード (Ja): キーワード (En): 作成者: Mamun, Md. Al, Islam, Ariful, Eto, Fumihiro, Sato, Tomohito, Kahyo, Tomoaki, Setou, Mitsutoshi メールアドレス: 所属:
URL	http://hdl.handle.net/10271/00003947

1 Review Article

2 **Mass spectrometry-based phospholipid imaging: methods and findings**

3

4 Md. Al Mamun¹, Ariful Islam¹, Fumihiro Eto¹, Tomohito Sato¹, Tomoaki Kahyo¹,
5 Mitsutoshi Setou^{1,2,3,*}

6 ¹Department of Cellular & Molecular Anatomy, Hamamatsu University School of
7 Medicine, 1-20-1 Handayama, Higashi-ku, Hamamatsu, Shizuoka 431-3192, Japan.

8 ²International Mass Imaging Center, Hamamatsu University School of Medicine, 1-20-1
9 Handayama, Higashi-ku, Hamamatsu, Shizuoka 431-3192, Japan.

10 ³Department of Systems Molecular Anatomy, Institute for Medical Photonics Research,
11 Preeminent Medical Photonics Education & Research Center, 1-20-1 Handayama,
12 Higashi-ku, Hamamatsu, Shizuoka 431-3192, Japan.

13 *Correspondence: setou@hama-med.ac.jp; Tel.: 053-435-2086; Fax: 053-435-2468

14 **Abstract**

15 **Introduction:** Imaging is a technique used for direct visualization of the internal structure
16 or distribution of biomolecules of a living system in a two-dimensional or three-
17 dimensional fashion. Phospholipids are important structural components of biological
18 membranes and have been reported to be associated with various human diseases.
19 Therefore, the visualization of phospholipids is crucial to understand the underlying
20 mechanism of cellular and molecular processes in normal and diseased conditions.

21 **Areas covered:** Mass spectrometry imaging (MSI) has enabled the label-free imaging of
22 individual phospholipids in biological tissues and cells. The commonly used MSI
23 techniques include matrix-assisted laser desorption ionization-MSI (MALDI-MSI),
24 desorption electrospray ionization-MSI (DESI-MSI), and secondary ion mass
25 spectrometry (SIMS) imaging. This special report described those methods, summarized
26 the findings, and discussed the future development for the imaging of phospholipids.

27 **Expert opinion:** Phospholipids imaging in complex biological samples has been
28 significantly benefited from the development of MSI methods. In MALDI-MSI, novel
29 matrix that produces homogenous crystals exclusively with polar lipids is important for
30 phospholipids imaging with greater efficiency and higher spatial resolution. DESI-MSI
31 has the potential of live imaging of the biological surface while SIMS is expected to image
32 at the subcellular level in the near future.

33 **Keywords:** Phospholipid; Mass spectrometry imaging; MALDI-MSI; DESI-MSI; SIMS
34 imaging.

35

36 **Highlights:**

- 37 1. Mass spectrometry imaging (MSI) is a powerful method for imaging specific
38 phospholipids (PLs) in tissues and cells.
- 39 2. The potential of MSI of either single or multiple PLs for the development of
40 therapeutic agents, biomarkers, and predictive factors for diseases is reviewed.
- 41 3. The current states of MALDI-MSI, DESI-MSI, and SIMS-MSI on tissue PL
42 imaging are assessed and discussed.
- 43 4. By image reconstruction, conventional 2D imaging can be applied in 3D PL
44 imaging.

45

46 **1. Introduction**

47 In biology, imaging refers to the technique used to visualize the internal structure or
48 biomolecules in tissues and cells of a living system in two- dimensional (2D) or three-
49 dimensional (3D) style without perturbing the structure. The history of imaging dates
50 back to 1895 when Wilhelm Roentgen discovered X-ray. X-ray was originally used in
51 medical imaging to create 2D image of internal organs in an X-ray film [1]. With the
52 advancement of computer vision and algorithms, several methods such as computed
53 tomography [2], magnetic resonance imaging [3], positron emission tomography [4] and
54 ultrasound [5] have been evolved to produce 2D as well as 3D image [6]. Besides
55 anatomical imaging, those techniques play important role in molecular imaging where
56 contrast agents are used for the noninvasive visualization, characterization, and
57 measurement of the biological processes in the living system [6,7,8]. Discovery of
58 electron microscope enabled the comprehensive visualization of cellular and subcellular
59 ultrastructures [9]. Some other microscopy-based labelled molecular imaging techniques
60 such as green fluorescent protein labelling [10], and immunohistochemistry [11] are used
61 to visualize the distribution map of protein molecules in tissue as well as cell structure.

62 Phospholipids (PLs) are one of the major structural components of biological membranes
63 [12,13] and play important roles in protecting the cells and organelles [14]. They also act
64 as signaling molecules [15] and precursors of many signaling mediators for various
65 biological processes [14,16]. An increasing amount of evidence indicates that the altered
66 level of PLs and their metabolites in tissues are associated with various human diseases
67 such as cancers [17], cardiovascular diseases [18], diabetes [19], Alzheimer's disease
68 (AD) [20,21], and autoimmune inflammatory diseases [22]. Therefore, it is important to
69 visualize individual PL species in tissue as well as in cellular level in order to explore the
70 underlying mechanism of cellular and molecular processes in normal and diseased
71 conditions. However, PLs in tissue sections cannot be imaged with conventional
72 molecular imaging techniques. Some staining methods such as Nile red [23], Oil Red O
73 [24,25] or osmium tetroxide [26] is commonly used to localize the PL fraction on frozen
74 tissue sections. However, these methods localize either the complete lipid fraction or only
75 one PL class on tissue sections, not individual PL species. Unlike immunohistochemistry
76 of proteins, there is no such protocol for individual PL imaging due to the lack of
77 antibodies or fluorescent probes.

78 Conventional mass spectrometry (MS) including liquid chromatography-MS (LC-MS)
79 has been extensively employed in lipidomics, particularly in the identification and
80 quantification of PLs in biological tissue [27,28]. Typical sample preparation protocol in
81 LC-MS includes the homogenization of tissue sample followed by lipid extraction
82 resulting in the loss of spatial information. LC-MS analysis of lipids extracted from
83 various anatomical regions of a certain tissue such as the brain is often investigated in
84 order to retain the spatial information [29,30]. However, it is a time-consuming process
85 and cannot resolve the microscopic anatomical regions because of the challenges in the
86 dissection and lipid extraction processes. In addition, the method requires a huge amount
87 of sample that limits the analysis of important clinical samples such as biopsy tissues.
88 Fortunately, MS has undergone tremendous development particularly in sample
89 preparation protocol and instrumentation enabling the analysis of biomolecules directly
90 from the thin tissue section to visualize individual molecule over the entire tissue [31,32].

91 So far, this method commonly known as imaging mass spectrometry (IMS) or mass
92 spectrometry imaging (MSI) has revolutionized the comprehensive imaging (2D and 3D)
93 of PLs in complex biological tissues. In this report, we focused on this technique in PLs
94 imaging including the methodologies and findings.

95

96 **2. Structure and classification of PL species**

97 PLs are diverse in chemical structures consisting of a hydrophilic head group and one or
98 more hydrophobic acyl chains attached to an alcohol moiety [14], and are commonly
99 referred to glycerophospholipids (GPLs) [33]. GPLs are esters of glycerol, fatty acids,
100 and phosphoric acid(s), where glycerol acts as the backbone. Two fatty acid chains are
101 generally present at the sn-1 and sn-2 positions, whereas the phosphate group is linked to
102 the sn-3 position of the glycerol backbone. The head group is attached to the phosphate
103 group(s), and its chemical nature can be diverse, leading to different GPLs. The most
104 common GPLs containing a single phosphate group are phosphatidylcholine (PC),
105 phosphatidylethanolamine (PE), phosphatidylinositol (PI), phosphatidylserine (PS),
106 phosphatidylglycerol (PG) and phosphatidic acid (PA). A subclass of GPLs is the
107 lysophospholipids (LPLs), in which a single fatty acid is present at either sn-1 or sn-2
108 position of the glycerol backbone. Examples of LPLs include lysophosphatidic acid
109 (LPA), lysophosphatidylcholine (LPC), lysophosphatidylethanolamine (LPE),
110 lysophosphatidylinositol (LPI), lysophosphatidylglycerol (LPG), and
111 lysophosphatidylserine (LPS). Diphosphatidylglycerol, historically known as cardiolipin
112 (CL), is a unique mitochondrial PL that contains two phosphate groups and four acyl
113 chains linked to the glycerol backbone (Table 1).

114 Various combinations of fatty acids and head group to the alcohol backbone, and their
115 oxidation products resulted in the remarkable structural diversity (Table 1) and biological
116 functions of the PLs molecules.

117

118

119

120

121

122

123

124

125

126

127

128

129

130

131

132

133 **Table 1: Names and structures of major phospholipids occurring in the living system.**

Major phospholipids	General structure
Phosphatidylcholine	$ \begin{array}{c} \text{O} \\ \parallel \\ \text{R}^2\text{-C-O-CH} \\ \\ \text{H}_2\text{C-O-C-R}^1 \\ \\ \text{H}_2\text{C-O-P-O-CH}_2\text{-CH}_2\text{-N}^+\text{(CH}_3\text{)}_3 \\ \\ \text{O}^- \end{array} $
Phosphatidylethanolamine	$ \begin{array}{c} \text{O} \\ \parallel \\ \text{R}^2\text{-C-O-CH} \\ \\ \text{H}_2\text{C-O-C-R}^1 \\ \\ \text{H}_2\text{C-O-P-O-CH}_2\text{-CH}_2\text{-NH}_2 \\ \\ \text{OH} \end{array} $
Phosphatidylserine	$ \begin{array}{c} \text{O} \\ \parallel \\ \text{R}^2\text{-C-O-CH} \\ \\ \text{H}_2\text{C-O-C-R}^1 \\ \\ \text{H}_2\text{C-O-P-O-CH}_2\text{-CH-NH}_3^+ \\ \qquad \qquad \qquad \\ \text{OH} \qquad \qquad \qquad \text{COO}^- \end{array} $
Phosphatidylinositol	$ \begin{array}{c} \text{O} \\ \parallel \\ \text{R}^2\text{-C-O-CH} \\ \\ \text{H}_2\text{C-O-C-R}^1 \\ \\ \text{H}_2\text{C-O-P-O-} \\ \qquad \qquad \qquad \\ \text{OH} \qquad \qquad \qquad \text{C}_6\text{H}_8\text{O}_5 \end{array} $
Phosphatidylglycerol	$ \begin{array}{c} \text{O} \\ \parallel \\ \text{R}^2\text{-C-O-CH} \\ \\ \text{H}_2\text{C-O-C-R}^1 \\ \\ \text{H}_2\text{C-O-P-O-CH}_2\text{-CH(OH)-CH}_2\text{(OH)} \\ \\ \text{OH} \end{array} $
Phosphatidic acid	$ \begin{array}{c} \text{O} \\ \parallel \\ \text{R}^2\text{-C-O-CH} \\ \\ \text{H}_2\text{C-O-C-R}^1 \\ \\ \text{H}_2\text{C-O-P-OH} \\ \\ \text{OH} \end{array} $
Cardiolipin	$ \begin{array}{c} \text{O} \qquad \qquad \qquad \text{OH} \qquad \qquad \qquad \text{O} \\ \parallel \qquad \qquad \qquad \qquad \qquad \qquad \parallel \\ \text{HO-P-O-CH}_2\text{-CH-CH}_2\text{-O-P-OH} \\ \qquad \qquad \qquad \qquad \qquad \qquad \\ \text{O} \qquad \qquad \qquad \text{O} \qquad \qquad \qquad \text{O} \\ \qquad \qquad \qquad \qquad \qquad \qquad \\ \text{CH}_2 \qquad \qquad \qquad \text{CH}_2 \qquad \qquad \qquad \text{CH}_2 \\ \qquad \qquad \qquad \qquad \qquad \qquad \\ \text{R}^1\text{-C-O-CH} \qquad \qquad \qquad \text{HC-O-C-R}^3 \\ \qquad \qquad \qquad \\ \text{R}^2\text{-C-O-CH}_2 \qquad \qquad \qquad \text{H}_2\text{C-O-C-R}^4 \\ \parallel \qquad \qquad \qquad \parallel \\ \text{O} \qquad \qquad \qquad \text{O} \end{array} $

134 N.B.: R¹, R², R³ and R⁴ indicate acyl chains of fatty acids.

135 **3. Methods of PLs imaging by MSI**

136 MSI is a powerful technique that allows the simultaneous imaging of hundreds of
137 biomolecules in thin tissue sections without extraction, purification or separation [34]. It
138 is a label-free molecular imaging method which was initially used to map proteins and
139 peptides in biological tissues [35]. In the last several years, this technique has been
140 utilized extensively in the visualization of individual PLs in a variety of human and
141 animal samples [36].

142 **3.1 Instrumentation for MSI**

143 Like conventional MS, the basic instrumentation of MSI includes (i) an ionization source
144 to generate ions from neutral molecules, (ii) a mass analyzer to analyze ions based on the
145 mass-to-charge ratio (m/z), and (iii) a detector to subsequently detect the ions and convert
146 into digital signals. The fundamental difference with the conventional MS is that it
147 collects ions directly from the surface area of a sample under controlled motion resulting
148 in the preservation of the spatial information.

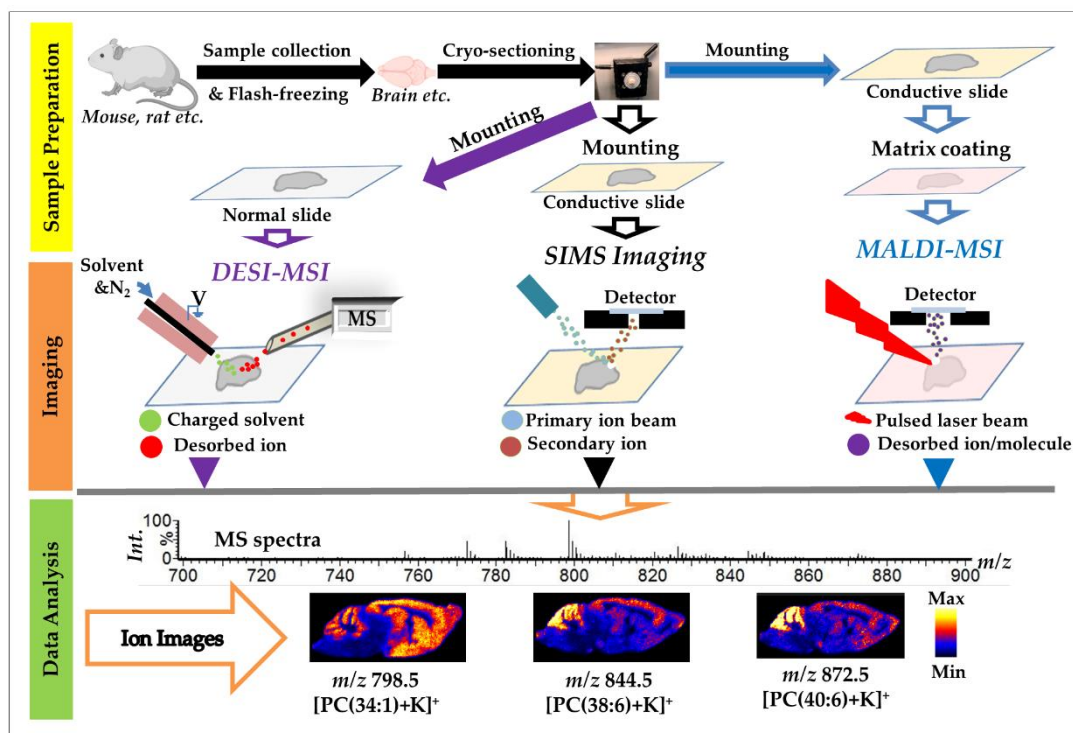
149 Numerous ionization sources originally developed for MS have been utilized further for
150 MSI analysis. Among the various ionization sources used for MSI, matrix-assisted laser
151 desorption ionization-MSI (MALDI-MSI) [37], desorption electrospray ionization-MSI
152 (DESI-MSI) [38], and secondary ion mass spectrometry (SIMS) imaging [39] are most
153 prominent. Several variants of MALDI-MSI include infrared-matrix-assisted laser
154 desorption electrospray ionization (IR-MALDESI) [40,41], atmospheric pressure
155 scanning microprobe MALDI (AP-SMALDI) [42], atmospheric pressure-MALDI-MSI
156 (AP-MALDI-MSI) [43], and matrix-free laser desorption ionization (LDI) techniques
157 such as nano-assisted laser desorption ionization-MSI (NALDI-MSI) [44] and desorption
158 ionization using through-hole alumina membrane-MSI (DIUTHAME-MSI) [45]. Some
159 other techniques such as laser ablation electrospray ionization (LAESI) [46], air flow-
160 assisted ionization-MSI (AFAI-MSI) [47], and easy ambient sonic spray ionization
161 (EASI) [48], have also been developed for imaging. The current report mainly focused
162 on the three major ionization techniques namely MALDI, DESI, and SIMS for PLs
163 imaging.

164 A variety of mass analyzers compatible with ionization sources are available for MSI
165 analysis. Time-of-flight (TOF) is the most common mass analyzer used for MSI due to
166 their high mass range, sensitivity and fragmentation capabilities in tandem MS. Ion trap
167 and quadrupole time-of-flight (QTOF) are also widely used in MALDI-MSI and DESI-
168 MSI. The use of Fourier-transform ion cyclotron resonance (FT-ICR) mass analyzer in
169 MALDI-MSI has significantly increased the molecular imaging with high mass resolution.
170 Each analyzer separates ions in a physically distinct mechanism, and has specific
171 advantages and limitations.

172

173

174



175

176

177

178

179

180

181

Figure 1: Overview of phospholipid imaging by mass spectrometry imaging. Tissue samples collected from human or animal sources are flash-frozen, cryosectioned, and thaw-mounted on a glass slide. For MALDI-MSI and SIMS imaging, the tissue section is generally mounted on indium tin oxide (ITO)-coated glass slide whereas DESI-MSI uses normal glass slide. Unlike MALDI-MSI, SIMS imaging and DESI-MSI do not require matrix-coating. The sample is placed onto a 2D moving stage and subjected to ionization usually in a raster fashion as the sample stage moves in x, y coordinates at a controlled speed. The ions are then analyzed based on the mass-to-charge ratio (m/z) in a mass analyzer. A detector subsequently detects those ions and converts them into digital signals. Results are displayed as mass spectra as well as two-dimensional ion-images. The mass spectra and the ion images shown here were acquired by DESI-MSI of mice brain sections.

182

183

184 3.2 Sample preparation for MSI

185 In MSI of PLs, careful sample preparation is crucial for successful imaging as the
186 polyunsaturated fatty acid containing-PLs (PUFA-PLs) are prone to oxidation.

187 3.2.1 Tissue sample preparation

188 *Collection of samples* – The use of thin sections of human and animal (usually mice and
189 rats) tissues is very common in PLs imaging. Human samples used for imaging include
190 the biopsy and the archived post-mortem tissues. Animals are usually euthanized by
191 cervical dislocation or using anesthetics prior to tissue collection. In order to preserve the
192 tissue anatomy and to halt the enzymatic degradation, tissues should be dissected rapidly

193 followed by immediate flash-freezing using powdered-dry ice or liquid nitrogen (Figure
194 1). The frozen tissues are then stored at -80 °C until sectioning.

195 *Cryo-sectioning*– Before slicing, frozen tissues are transferred into a cryostat chamber
196 and left for 15 – 20 minutes at – 10 °C to – 20 °C to equilibrate to the sectioning
197 temperature. Tissue block is affixed to the stage of a cryostat machine using an embedding
198 media and then sliced at a thickness of around 5 – 20 µm. For 3D MSI, a series of serial
199 sections are collected with minimal error and registered carefully. During sectioning,
200 optimized temperature, usually at – 20 °C (can vary depending on the type of tissue), must
201 be maintained in the cryostat. Particular care should be taken when using optimal cutting
202 temperature embedding media (OCT) or other embedding media containing polymer as
203 they cause serious contamination reducing the quality of the spectra. The thickness of the
204 section should be as thin as possible to achieve higher quality spectral data in MALDI-
205 MSI [49], although DESI-MSI has the flexibility regarding the sample thickness.

206 *Sample pre-treatment* – For MALDI, the tissue section is generally thaw-mounted on an
207 indium tin oxide (ITO)-coated glass slide followed by a homogenous coating with a
208 suitable matrix solution allowing the formation of co-crystals between the matrix
209 molecules and the analytes. The matrix molecules must have the property of absorbing
210 laser energy to aid in the ionization process. Various matrix compounds have been
211 developed due to the fact that a single matrix does not work for all PLs. For instance, 2,5-
212 Dihydroxybenzoic acid is commonly used to image PC molecules [50,51] in positive ion
213 mode while 9-aminoacridine is used for imaging various PLs including PI, PG, PS, PA
214 and CL in negative ion mode [52]. Other matrices that have been used for the imaging of
215 PLs include 2,5-dihydroxyacetophenone [53], α -cyano-4-hydroxycinnamic acid [50],
216 graphene oxide [54], and 1,6-Diphenyl-1,3,5-hexatriene [55]. The matrix can be sprayed
217 either manually (e.g., using artistic air brush) or automatically (e.g., using TM-SprayerTM
218 manufactured by HTX Technologies, and ImagePrep manufactured by Bruker Daltonics
219 Inc.) [56].

220 Unlike MALDI, DESI uses normal glass slide for tissue mounting and does not require
221 sample pre-treatment reducing the time significantly for sample preparation.

222 For SIMS imaging, the tissue section is generally transferred onto the ITO-coated glass
223 slide and does not require matrix coating. Unfortunately, the high energy primary ion
224 beam used in typical SIMS causes increased fragmentation of the PLs resulting in the
225 poor molecular ion yield. In order to reduce the fragmentations, several approaches for
226 sample preparation such as matrix enhancement (similar to MALDI protocol) and surface
227 metallization (coating with a thin layer of gold or silver) have been developed [57].

228 **3.2.2 Sample preparation for single-cell imaging**

229 PLs imaging at the cellular level has been made possible by SIMS imaging as it offers the
230 capability of resolving very small features which can be as low as a hundred nanometers.
231 Sample for single-cell analysis includes the isolated cells from the specimen or cultured
232 cell. Unfortunately, live cells cannot be analyzed directly in SIMS as it works under a
233 high vacuum condition. Generally, cells are extracted or grown on an appropriate
234 substrate such as silicon wafer or gold-coated silicon wafer [58] followed by fixation to
235 minimize sample degradation. Two fixation methods are commonly applied: (i) chemical
236 fixation using glutaraldehyde, and (ii) cryofixation. A cryofixation method, namely

237 plunge fixation, has been shown to be advantageous for single-cell lipid imaging [59]. In
238 plunge freezing, samples are stored in liquid nitrogen at -196 °C after washing by a
239 mixture of propane and isopentane (3:1). Interestingly, enhanced signal intensity for PLs
240 has been reported when matrix solution is added on the cell surface prior to the fixation
241 [58]. After fixation, frozen samples are freeze-dried and stored until analysis.

242 **3.3 Analysis by MSI**

243 To minimize the degradation or oxidation of the PLs, imaging should be performed as
244 soon as possible once the sample is ready for analysis. The sample is placed onto a 2D
245 moving stage and subjected to ionization either in positive or negative ion mode. Ions are
246 collected from the surface usually in a raster fashion as the sample stage moves in x, y
247 coordinates at a controlled speed. The ions are then sent into the mass analyzer for
248 analysis and subsequently detected by the detector system.

249 PLs are a large group of molecules and show diversity in ion production. PC and PE are
250 typically ionized in positive ion mode as protonated/sodiated/potassiated adducts while
251 PS, PA, PI, and PG are ionized in negative ion mode as deprotonated ions in the mass
252 range of m/z 700 – 900. LPLs are detected either in positive or negative ion mode in the
253 mass range of m/z 400 – 600, on the other hand, singly charged CLs are usually detected
254 in the negative ion mode in the mass range of m/z 1000 – 1600.

255 MALDI is a widely used soft ionization process that primarily produces singly-charged
256 ions in both positive and negative ion modes. In this method, the matrix-coated sample
257 surface is irradiated by pulsed laser causing the rapid excitation and heating of the matrix
258 molecules [60,61] (Figure 1). The heated molecules undergo evaporation resulting in the
259 desorption of neutral and charged analytes, matrix molecules, analyte-matrix, and matrix-
260 matrix clusters, all under the vacuum conditions. Ionization of the analytes are thought to
261 occur during the desorption process, or in the expanding plume through the charge
262 transfer between the excited matrix molecules and the neutral analytes. Ultraviolet lasers
263 such as frequency-tripled Nd:YAG lasers (355 nm) are commonly used for MALDI-MSI
264 as they are strongly absorbed by the matrix molecules [62].

265 Unlike MALDI, DESI works in an open environment at atmospheric pressure. In DESI,
266 a beam of charged microdroplets of solvent coupled with a nebulizer nitrogen gas is
267 directed continuously onto the tissue surface where molecules are extracted, ionized and
268 desorbed into the mass spectrometer for analysis [63] (Figure 1). Methanol (usually 98%)
269 is commonly sprayed at a flow rate of 2 — 5 $\mu\text{L}/\text{min}$ using a solvent pump, and a capillary
270 voltage of 2 — 4.0 kV is generally applied to charge the solvent. A 2-D stage moves the
271 tissue at a controlled speed to record the mass spectra from different spatial coordinates.
272 The spatial resolution of DESI is lower (can range between 50—200 μm) than that of
273 MALDI (typically <50 μm). However, nano-DESI can offer much higher spatial
274 resolution (better than 10 μm) [64,65,66]. Prior to the analysis, optimization of several
275 parameters such as solvent composition, solvent flow rate, gas flow rate, capillary voltage,
276 cone voltage, inlet temperature, and the geometry of the sprayer is required in order to
277 obtain the highest desorption and ionization as well as the best spatial resolution of the
278 ion image [67,68].

279 Conventionally, SIMS uses a hard ionization technique where the tissue surface is
280 bombarded with a focused high energy primary ion beam, causing desorption of

281 secondary ions into the mass analyzer. It operates either in dynamic or static modes, while
282 the latter is used for PLs imaging as the intact molecular ions are typically detected under
283 that condition. The emergence of cluster ion sources (e.g., C₆₀⁺, Bi₃⁺, and Au₃⁺) as a
284 primary ion beam has significantly improved the PLs imaging with high sensitivity [57].
285 Like MALDI, ionization events in SIMS occur under the vacuum conditions.

286 For single-cell analysis, freeze-dried cells are typically subjected to SIMS imaging.
287 Interestingly, the increased signal intensity of PLs was observed when the sample is
288 analyzed in frozen-hydrated conditions where the cryo-fixed cells are kept frozen with a
289 liquid nitrogen-cooled stage during the analysis [69,57].

290 **3.4 Data analysis**

291 MSI data are multidimensional, and usually processed by in-built software visualizing as
292 mass spectra (a plot of intensity vs. m/z), and 2D-ion images corresponding to each ion
293 signal (Figure 1). In 3D MSI, suitable 2D ion images acquired from a series of serial
294 sections are combined to construct a 3D image. Each pixel of the ion image contains a
295 mass spectrum of all molecules detected at that irradiated/sprayed area. Data
296 normalization to the total ion current is often used to eliminate artifacts. MSI has the
297 strength of combining (e.g., overlay, merge etc.) an ion image corresponding to a certain
298 signal with the microscopic data (e.g. H&E stained image) of the same or serial tissue
299 section allowing the interpretation of the spatial distribution within the histological
300 context. Mass spectra from different regions of interest (ROIs) of an ion image can be
301 extracted and compared. Multivariate analysis methods (MVA), particularly, principal
302 component analysis (unsupervised method) and partial least-squares regression
303 (supervised method) are widely used to classify or differentiate between ROIs or samples
304 by reducing the dimensionality of the MSI data. MVA is often used in combination with
305 discriminant analysis to examine how well the ROIs or samples are differentiated.
306 Statistical analyses such as t-tests and ANOVA are performed to evaluate whether the
307 observed distributional changes are significant. For biomarker discovery, a receiver
308 operator characteristic curve analysis is often performed that calculates the sensitivity and
309 specificity of individual ions.

310 Unambiguous molecular assignment to an m/z of interest is an important task in MSI. A
311 careful assignment is highly recommended since an m/z value often presents a number of
312 different molecular ions. In addition, two or more PLs can be detected at a single m/z
313 value in the spectra as PLs show diversity in their head group, acyl chain moieties, and
314 adduct forms. The tentative assignments of PLs are performed by matching the observed
315 m/z value in the mass spectra to the reported literature or database of known compounds
316 within an acceptable mass error range (typically 1-20 ppm, varies with the mass resolution
317 of the analyzer). Several online databases such as human metabolome database
318 (<https://hmdb.ca/>) [70], and lipid map (<https://www.lipidmaps.org/>) [71] are dedicated for
319 this purpose. For unambiguous assignments, tandem mass spectrometry analysis (e.g.,
320 on-tissue MS/MS, LC-MS/MS of lipid extracts) is routinely performed where individual
321 lipid species yield characteristic fragment ions (e.g., fragments specific to the head groups,
322 sn-1 and sn-2 fatty acyl groups etc.) [72]. The fragmentation patterns of the ion of interest
323 are compared with those of a pure compound analyzed under the identical conditions.
324 Immunohistochemical analyses of protein(s) related to the PL of interest are often
325 performed for further confirmations of the specific PL assignment [73,74].

326

327 **4. Reports on PLs imaging by MSI**

328 MSI has been employed extensively to explore the spatial distribution of PL species in a
329 variety of biological samples [75]. MALDI-MSI is the most widely used techniques for
330 PLs imaging followed by the DESI-MSI and SIMS imaging. By far the most detected PL
331 species are the PCs while the most imaged tissues are brain and tumors.

332 **4.1 MSI revealed the region-specific distributions of individual PLs**

333 Distribution of specific PLs in different normal anatomical locations of biological tissues
334 has been extensively studied. MALDI-MSI allowed visualizing the cell-selective
335 distribution of polyunsaturated fatty acid-containing PCs (PUFA-PCs) in mouse brain:
336 arachidonic acid-containing PCs and DHA-PCs were distributed in the hippocampal
337 neurons and cerebellar Purkinje cells, respectively [76]. Two PLs, PI(38:4) and PC(36:1)
338 were preferentially localized to the gray matter while PC(32:0) were preferentially
339 localized to the white matter of rat brain [51]. PLs imaging in the human term placenta
340 showed the differential distribution of PC(16:0_20:4) between the stem and terminal villi
341 [77]. Two PC molecules, PC(16:0_18:2) and PC(16:0_18:1) were detected as the
342 dominant molecules in the human gastric mucosa near the fundic glands [78]. DESI-MSI
343 was capable of imaging 1-O-alkyl phosphatidylethanolamines and phosphatidylserines,
344 PE (18:1e/18:1), and PS (18:1e/18:1) in a thin ring in the outermost region of the human
345 lens [79]. Some other MALDI-MSI studies showed the distributions of PLs in various
346 biological tissues including rat brain [80,81,82], heart [83], liver [84], mouse kidney [85],
347 lung [86] and human lens [87]. ToF-SIMS imaging revealed the distribution of some
348 specific PLs in the sections of the mouse brain [88], rat brain [89] and human skeletal
349 muscle [90]. While the most imaged samples in the literature are tissues, several studies
350 applied MALDI-MSI to profile PLs distribution in the whole body of some species
351 including *Caenorhabditis elegans* [91], and *Drosophila melanogaster* [92].

352 **4.2 PLs imaging determined the margin of diseased tissue**

353 MSI has successfully revealed the altered distribution of some specific PLs in several
354 diseased tissues thereby discriminating between diseased and healthy tissues [93,94]. This
355 power of demarcation is of great help for the successful surgery of diseased tissue,
356 particularly the tumors. In a MALDI-MSI study, our group reported that PC (36:1) was
357 highly abundant in human breast cancer tissues than in the references [73] Margulis et al.
358 used DESI-MSI and reported the distinct distribution of PG(18:1_16:0) and the relatively
359 higher distribution of PS(18:1_18:0) and PI(18:0_20:4) in the human basal cell carcinoma
360 tissue than in the normal skin [95]. Distinct distributions of PLs including PI(18:0/20:4)
361 were seen in human seminoma and adjacent normal tissues [94]. In a study, 37 resected
362 hepatocellular carcinoma tissues were analyzed by MALDI-MSI and revealed an increase
363 of PC(16:0_16:1) and a decrease of LPC(16:0) in the cancerous region than in the normal
364 region [96]. MALDI-MSI showed a higher accumulation of stearic acid and arachidonic
365 acid-containing PI, PI(18:0_20:4), in the thickened wall than in the thinned wall of
366 intracranial aneurysms [97]. Imaging of the ischemic rat brain revealed the production of
367 LPC(16:0) in the area of focal cerebral ischemia [98].

368 **4.3 PLs imaging showed the potentiality to the therapeutics discovery**

369 A large number of MSI studies were performed to examine the changes of PLs level in
370 tissues after a certain intervention in animal or insect, and thereby revealed the promising
371 therapeutic agents for diseases. Recently, our group imaged PLs in the dorsal root
372 ganglion (DRG) of mice after sciatic nerve transection (SNT) using MALDI-FTICR
373 imaging at a spatial resolution of 25 μ M. The study showed that the arachidonic acid-
374 containing PC (AA-PC), PC(16:0_20:4) highly increased while other two PCs and one
375 PA(36:2) molecule decreased in the DRG following nerve transection [99]. LPA, an
376 initiator of neuropathic pain, is generated from PA by phospholipase A2 enzymes [100]
377 speculating that PA(36:2) is consumed to produce LPA [99]. Thus, the study suggested
378 the potential use of LPA blocker for the treatment of neuropathic pain [99]. Our group
379 employed MALDI-MSI and showed that a stearate and docosahexaenoic acid (DHA)
380 containing PC (DHA-PC), PC(18:0_22:6), depleted in the grey matter of a post-mortem
381 human AD brain [101] which was in excellent agreement with another study that revealed
382 the improved memory function and distribution levels of brain DHA in senescence-
383 accelerated mice P8 (SAMP8 mice), a model of dementia, supplemented with green nut
384 oil (a rich source of α -linolenic acid) or DHA [102]. Recently, we used DESI-MSI
385 technique to image the DHA-PCs in the brain of SAMP8 mice fed with green nut oil or
386 DHA. SAMP8 mice brain showed the lower distribution of PC(16:0_22:6), and
387 PC(18:0_22:6) compared to that of wild type mice. Interestingly, green nut oil or DHA
388 treatment restored the decreased distribution of PC(16:0_22:6) and PC(18:0_22:6) in the
389 brain of SAMP8 mice [72] suggesting the potential use of DHA and green nut oil in the
390 prevention and treatment of dementia. Philipsen et al. examined the distribution of some
391 individual phospholipids in Drosophila brain after the administration of cocaine and
392 methylphenidate by ToF-SIMS imaging with a spatial resolution around 3 μ M and
393 revealed the possible involvement of brain lipids in learning and memory. Before
394 treatment, two PCs, PC(34:1) and PC(34:2) were found to be abundant in the central brain
395 while PE(34:1) and PI(36:4) were distributed throughout the brain. Cocaine
396 administration largely changed the distribution of those PLs: PCs became more abundant
397 in the central brain and optical lobe areas whereas the overall intensities of PE and PI
398 decreased [103].

399 **4.4 MSI identified PLs as a biomarker and predictive factor of diseases**

400 MSI of PLs showed the promising power to the discovery of cancer biomarker and
401 predictive factor of tumor recurrence which can potentially contribute to the improved
402 disease management and monitoring of the disease progression. In a MALDI-MSI study,
403 PC(16:0_16:1) was revealed as a novel biomarker in colorectal cancer [104]. PC (32:1)
404 is highly abundant in recurrent triple-negative breast cancer (TNBC) tissues compared to
405 the non-recurrent TNBC tissues making it as a potential predictive factor of TNBC
406 recurrence [105]. High resolution-MALDI-MSI revealed the lower expression of
407 LPC(16:0/OH) in prostate cancer than that in the benign prostate epithelium of human.
408 These differences in expression of PLs will potentially help predict prostate cancer
409 aggressiveness, and provide novel insights into the lipid metabolism in prostate cancer
410 tissue [106]. In DESI-MSI study, lipids including several individual PCs, PGs and CLs
411 were identified as biomarkers as well as predictive factors of serous ovarian cancer [93].
412 This methodology was utilized in classifying disease status, different subtypes and grades
413 of several cancers including human bladder carcinomas [107], gliomas [108], renal cell
414 carcinomas [109], and breast cancer [110]. Furthermore, Mao et al. showed the

415 application of AFAI-MSI in the rapid classification of human breast tumors based on the
416 abundance of lipids including PLs [111].

417 **4.5 Potential mechanism of cancer invasion revealed by PLs imaging**

418 Membrane fluidity is thought to largely depend on the fatty acyl species linked to the PCs
419 [112]. Compositional changes in the acyl chains may thus contribute to the altered fluidity
420 influencing the behavior of the cancer cells, such as invasion and metastasis. Mapping of
421 superficial-type pharyngeal carcinoma tissue sections from five human patients showed
422 the higher distributions of three AA-PCs, PC(16:0_20:4), PC(18:1_20:4) and
423 PC(18:0_20:4) in the subepithelial invasive region indicating the potential role of AA-
424 PCs in the invasion mechanism [113].

425 **4.6 CLs imaging**

426 It is now clear that MSI has shown tremendous progress on PCs imaging in the last several
427 years. PCs are the most abundant molecules in the membranes and also dominate the mass
428 spectra due to their higher ionization efficiency than the other PL species. Unfortunately,
429 these highly abundant molecules contribute to the ion suppression of some other PLs of
430 low abundance. Due to this fact, the most reported PLs in the literature are the PCs,
431 followed by LPLs and CLs.

432 CLs are unique mitochondrial PLs that play important structural as well as functional
433 roles in bioenergetics and signaling [114]. They exist in a relatively small amount with
434 remarkable diversification and are difficult to detect due to the ion suppressive effect of
435 the highly abundant molecules present on the tissue surface. So far, a decrease level of
436 CLs were reported in the kidney cortex of non-alcoholic steatohepatitis mice using the
437 conventional MALDI-MSI protocol [115]. Several methods have been developed for CLs
438 imaging by reducing or eliminating the ion suppressive effects. Amoscato et al. showed
439 that the treatment of the tissue surface (prior to MALDI-MSI) with phospholipase C and
440 1-ethyl-3-[3-(dimethylamino)propyl]-carbodiimide hydrochloride (EDC) eliminates the
441 ion suppressive effects by removing the highly abundant phosphatidylcholine head
442 groups and cross-linking the accessible carboxyl/amino-containing molecules on the
443 tissue, respectively [116]. Using this approach, authors successfully mapped multiple CLs
444 and demonstrated a nonrandom distribution of PUFA and non-PUFA containing CLs in
445 different anatomical locations of the male rat brain. Interestingly, the habenular
446 nuclear/dorsal third ventricle and lateral ventricle areas of the brain showed a robust
447 signal for CLs and were defined as the CL “hot spot” [116]. By employing similar
448 methods, it was revealed that the traumatic brain injury in rats resulted in the early
449 depletions in polyunsaturated CLs in the contusional cortex, ipsilateral hippocampus, and
450 thalamus [117]. Recently, Yang et al. demonstrated an effective MALDI-MSI method for
451 CLs mapping based on the sample preparation with norharmane matrix that does not
452 require additional digestion procedure [118]. DESI-MSI showed the capability of direct
453 CLs imaging in normal and cancer tissues. Several individual CLs with a smaller number
454 of double bonds were shown to significantly increased in v-myc avian myelocytomatosis
455 viral oncogene homolog (MYC)-induced lymphomas compared with normal tissue [119].
456 Furthermore, DESI-MSI identified cardiolipins as a molecular signature of mitochondria-
457 rich thyroid oncocytic tumors [120].

458 **4.7 Imaging of oxidized PLs**

459 PUFA- containing PLs (PUFA-PLs) in the membrane undergoes oxidation by various
460 enzymes or reactive oxygen species producing oxidized PLs. Oxidized PLs are highly
461 bioactive molecules having both pro-inflammatory and anti-inflammatory effects and are
462 now considered as markers of biological oxidative stress [121]. Oxidized PLs in human
463 and animal tissues have been extensively studied by the LC-MS techniques [122].
464 Recently, there is a growing interest in imaging these modified PLs to discover biomarker
465 for disease states and to advance the understanding of pathology. MALDI-MSI revealed
466 a decrease of oxidizable PUFA-PLs including PS(18:0_22:6) in traumatic brain injury
467 [75]. However, no reports on oxidized PLs imaging have been demonstrated using that
468 method. So far, DESI-MSI identified several oxidized-CL species in mitochondria-rich
469 thyroid oncocytic tumors [120].

470 **4.8 Imaging of single-cell PLs**

471 MALDI-MSI is capable of imaging at a spatial resolution less than 50 μM [99] and has
472 been applied in PLs imaging at the cellular level. In a MALDI-MSI approach, flow
473 cytometry-sorted single multiple myeloma cells and normal plasma cells were imaged
474 with 5 μM laser ablation diameter and revealed a decrease of PC(16:0_20:4) in the
475 malignant cells [123]. AP-MALDI imaging with 7 μM pixel size detected PC(32:1) and
476 PC(34:1) primarily in the center of the HeLa cells where a large volume of membranes
477 are expected [124]. However, these methods revealed only the gross PLs distribution on
478 the cell surface.

479 So far, SIMS offers spatial resolution at a nanometer scale which is suitable for single-
480 cell imaging. Unfortunately, PLs undergo severe fragmentations by the high energy
481 primary ion beam resulting in the decreased spectral and image quality. Fragments of the
482 phosphocholine head group are commonly seen in the mass spectra of SIMS, and they
483 are often used to record the total PCs distribution. Ostrowski et al. employed TOF-SIMS
484 under frozen-hydrated conditions to study the changes in the membrane lipid distribution
485 during mating of *Tetrahymena thermophila* and observed a significant decrease of
486 phosphocholine head group fragment along the conjugation junction [125].

487 Introduction of cluster ion sources and modifications in the sample preparation protocol
488 have been developed discussed previously to reduce the fragmentations. Addition of
489 matrix increased the signal intensity of several PCs including PC(34:1) on single-cell
490 surface cultured on gold-coated silicon wafers [58]. Unfortunately, the crystals formed
491 by matrix-coating mask some structural details on the cell surface, resulting in the poor
492 image quality.

493 **4.9 3D imaging of PLs**

494 With the advancement of the image reconstruction method and the high-throughput
495 analysis, MSI showed the ability to generate 3D images of PLs distribution in an entire
496 organ or tissue. Patterson and coworkers developed a robust 3D MSI method using open-
497 source software and revealed the distributions of LPC and PC molecules in human and
498 mice carotid atherosclerosis tissues [126]. 3D MALDI-MSI technique has been applied
499 to map PLs in newly fertilized zebrafish embryos: PCs were mostly distributed inside the
500 yolk as well as in the blastodisc, while PEs and PIs were distributed minimally inside the
501 yolk [127]. Paine et al. performed 3D MALDI-MSI on whole brains from a mouse model
502 of human medulloblastoma and identified several PA, PE, PS, and PI molecules

503 associated with the metastasis [128]. DESI-MSI and SIMS imaging have also been
504 utilized for 3D imaging of PLs in various tissues that include mice brain [129],
505 glioblastoma xenograft [130], and *Aedes aegypti* ovarian follicles [131].

506

507

508

509 **5. Conclusions**

510 PLs imaging in complex biological tissues and cells has been revolutionized by the
511 development of label-free MSI techniques. MALDI-MSI, DESI-MSI and SIMS imaging
512 are the widely used MSI methods for the imaging of specific PLs, so far. MSI revealed
513 the region-specific distributions of specific PLs in various tissues. Imaging of individual
514 PLs demarcated the margins of cancers and contributed to the discovery of potential
515 therapeutics, biomarkers, and predictive factors of diseases. Interestingly, the potential
516 role of PLs in cancer invasion has been revealed by this technique. The abundance and
517 the higher ionization efficiency of PCs contribute to the suppression of other PLS
518 including CLs and oxidized PLs. Development in the sample preparation protocol enabled
519 the successful imaging of CLs by reducing the ion suppression.

520

521 **6. Expert opinion**

522 MSI is a powerful method that has the capability of untargeted analysis of hundreds of
523 molecules simultaneously in complex biological tissues and cells without labelling. These
524 unique features made it a valuable tool for the visualization of proteins [132], lipids [36],
525 nucleotides [133], neurotransmitters [134], small metabolites [135], and exogenous
526 compounds [136] in a wide range of biological samples. It has become an indispensable
527 tool for the imaging of individual PLs so far and greatly contributed to explore biomarkers
528 as well as altered lipid distribution in various diseased states. However, there are many
529 challenges in MSI of PLs exist.

530 Because of the variations of the acyl chains and the head groups, thousands of PL species
531 could be present in a living cell. The head group attached to the phosphoric acid as well
532 as the acyl chains of the glycerol backbone are detected and identified in tandem mass
533 spectrometry. Unfortunately, the positional analysis of these chains (acyl chains specific
534 to sn-1 and sn-2) is not possible in the current situation. In addition, on-tissue tandem
535 MSI is often problematic due to the less sensitivity and the difficulty to isolate a target
536 molecular ion from a myriad of molecules of the complex tissue sections. Therefore,
537 imaging of PLs warrants further advancement of the mass analyzer for positional analysis
538 of acyl chains and on-tissue MS/MS.

539 MSI is a surface analysis method and provides only the semi-quantitative information of
540 the analytes. Although a lot of progress have been made in the development of methods,
541 quantification is still one of the greatest challenges in MSI. A strategy for quantitative
542 analysis could be the development of calibration curves using internal standards.

543 MALDI-MSI offers a better sensitivity for PLs detection than the other currently used
544 MSI techniques. However, the choice of a matrix and the spray conditions directly affect
545 the ionization efficiency and spatial resolution. A lot of efforts have been made to explore
546 novel matrix and optimized spray conditions for successful imaging. Our group
547 developed a two-step matrix application technique namely “spray-droplet method” that
548 produce homogenous layer with minute crystals resulting in the improved ionization
549 efficiency for MALDI-MSI [137]. Further development of matrix or alternative to the
550 matrix that form homogenous crystals exclusively with polar lipids will potentially
551 contribute to the PLs imaging with higher ionization efficiency and higher spatial
552 resolution. The use of nanoparticle instead of matrix enabled the visualization of several
553 PLs at an improved resolution (15 μm) in mammalian tissues [138].

554 DESI-MSI, a relatively new and nondestructive imaging method, has attracted much
555 attention due to its capability of matrix-free simple analysis. In our experience, DESI-
556 MSI is a suitable technique for analyzing small molecules [139,140,141] although it’s
557 spatial resolution and the ionization efficiency for PLs are lower than that of MALDI-
558 MSI. DESI-MSI has a great potential of live imaging of biological surface molecules in
559 clinical settings since it does not require any special sample preparation. Higher spatial
560 resolution can be achieved through the advancement of the sprayer conditions (such as
561 solvent flow rate, gas flow rate etc.) and the geometry of the ionization chamber while
562 ionization efficiency for PLs can be improved by exploring the right solvent composition.

563 Nowadays, the need for PLs imaging at the sub-cellular level is increasing. Unlike tissue
564 section imaging, single-cell imaging presents a great challenge as it requires techniques
565 with high spatial resolution as well as high sensitivity because of the microscopic size
566 and extremely small volume of analytes in a single cell. In DESI-MSI, pixel size is
567 typically in the range of 50–200 μm , and thus single-cell structures cannot be resolved
568 with this spatial resolution. Single-cell imaging by MALDI-MSI has revealed only the
569 gross distributions of PLs. So far, SIMS has shown the capability of resolving features at
570 the nanometer scale which allows for the imaging at the sub-cellular level. Unfortunately,
571 it is difficult to detect PLs by this technique since fragmentation occurs during analysis.
572 Some advancement including the use of cluster ion sources and the sample analysis under
573 frozen-hydrated state significantly improved the PLs imaging.

574 Although MSI was primarily developed for 2D imaging, it has been applied for 3D
575 imaging that significantly enhanced our understanding of the molecular processes.
576 However, the current methodology for 3D MSI is laborious and time consuming.
577 Interestingly, an automated 3D DESI-MSI method has been demonstrated for rapid
578 analysis. In this technique, a robotic slide loader is installed to autonomously mount and
579 change slides on the sample stage while the 2D ion images are automatically constructed
580 and aligned to generate a 3D image [130].

581 Imaging of low abundance PLs including the CLs and oxidized PLs is still in its infancy.
582 Methodological developments that reduce the ion suppression effect, and increase the
583 sensitivity are warranted for the imaging of these molecules.

584

585

586 **7. Acknowledgements**

587 This work was supported by MEXT/JSPS KAKENHI (Grant Number JP15H05898B1),
588 AMED (Grant Number JP20gm0910004), JSPS KAKENHI (Grant Number
589 JP18H05268), and MEXT Project for promoting public utilization of advanced research
590 infrastructure (Imaging Platform) under grant number JPMXS0410300220, Japan.

591

592

593

594

595 **8. References**

- 596 1. William G. Bradley. History of medical imaging. Proceedings of the American
597 Philosophical Society. 152(3), 349–361(2008).
- 598 2. Kalender, W.A. X-ray computed tomography. Phys. Med. Biol. 51(13), R29-
599 43(2006).
- 600 3. Grover, V.P.B.; Tognarelli, J.M.; Crossey, M.M.E.; Cox, I.J.; Taylor-Robinson,
601 S.D.; McPhail, M.J.W. Magnetic resonance imaging: principles and techniques:
602 lessons for clinicians. J. Clin. Exp. Hepatol. 5, 246–255 (2015).
- 603 4. Unterrainer, M.; Eze, C.; Ilhan, H., et al. Recent advances of PET imaging in
604 clinical radiation oncology. Radiat. Oncol. 15, 1–15 (2020).
- 605 5. Seo, J.; Kim, Y. sun. Ultrasound imaging and beyond: recent advances in medical
606 ultrasound. Biomed. Eng. Lett. 7, 57–58 (2017).
- 607 6. Pysz, M.A.; Gambhir, S.S.; Willmann, J.K. Molecular imaging: current status and
608 emerging strategies. Clin. Radiol. 65, 500–516 (2010).
- 609 7. Deshpande, N.; Needles, A.; Willmann, J.K. Molecular ultrasound imaging:
610 current status and future directions. Clin. Radiol. 65, 567–581 (2010).
- 611 8. Wu, M.; Shu, J. Multimodal Molecular Imaging: Current Status and Future
612 Directions. Contrast Media Mol. Imaging. (2018).
- 613 9. Porter, K.R.; Claude, A.; Fullam, E.F. A study of tissue culture cells by electron
614 microscopy: Methods and preliminary observations. J. Exp. Med. 81, 233–246
615 (1945).
- 616 10. Prendergast, F.G.; Mann, K.G. Chemical and physical properties of aequorin and
617 the green fluorescent protein isolated from *Aequorea forskålea*. Biochemistry. 17,
618 3448–3453 (1978).
- 619 11. de Matos, L.L.; Trufelli, D.C.; de Matos, M.G.L.; Pinhal, M.A. da S.
620 Immunohistochemistry as an important tool in biomarkers detection and clinical
621 practice. Biomark. Insights. 5, 9–20 (2010).
- 622 12. Cevc, G. Phospholipids Handbook; CRC Press, 2018;
- 623 13. Chapman, D. Phospholipid bilayers physical principles and models. Cell Biochem.
624 Funct. 6, 147–148 (1988).
- 625 14. Cai, T.; Yang, F. Phospholipid and Phospholipidomics in Health and Diseases. In;
626 Springer, Singapore, pp. 177–202 (2018).

- 627 15. Birge, R.B.; Boeltz, S.; Kumar, S.; et al. Phosphatidylserine is a global
628 immunosuppressive signal in efferocytosis, infectious disease, and cancer. *Cell*
629 *Death Differ.* 23, 962–978 (2016).
- 630 16. Deigner, H.P.; Hermetter, A. Oxidized phospholipids: Emerging lipid mediators
631 in pathophysiology. *Curr. Opin. Lipidol.* 19, 289–294 (2008).
- 632 17. Cheng, M.; Bhujwalla, Z.M.; Glunde, K. Targeting phospholipid metabolism in
633 cancer. *Front. Oncol.* 6, 266 (2016).
- 634 18. Ashraf, M.Z.; Kar, N.S.; Podrez, E.A. Oxidized phospholipids: Biomarker for
635 cardiovascular diseases. *Int. J. Biochem. Cell Biol.* 41, 1241–1244 (2009).
- 636 19. Chang, W.; Hatch, G.M.; Wang, Y.; Yu, F.; Wang, M. The relationship between
637 phospholipids and insulin resistance: From clinical to experimental studies. *J. Cell.*
638 *Mol. Med.* 23, 702–710 (2019).
- 639 20. Kosicek, M.; Hecimovic, S. Phospholipids and Alzheimer’s disease: Alterations,
640 mechanisms and potential biomarkers. *Int. J. Mol. Sci.* 14, 1310–1322(2013).
- 641 21. Kao, Y.-C.; Ho, P.-C.; Tu, Y.-K.; Jou, I.-M.; Tsai, K.-J. Lipids and Alzheimer’s
642 Disease. *Int. J. Mol. Sci.* 21, 1505(2020).
- 643 22. Cas, M.D.; Roda, G.; Li, F.; Secundo, F. Functional lipids in autoimmune
644 inflammatory diseases. *Int. J. Mol. Sci.* 21(2020).
- 645 23. van Goor, H.; Gerrits, P.O.; Grond, J. The application of lipid-soluble stains in
646 plastic-embedded sections. *Histochemistry.* 85, 251–253 (1986).
- 647 24. Mehlem, A.; Hagberg, C.E.; Muhl, L.; Eriksson, U.; Falkevall, A. Imaging of
648 neutral lipids by oil red O for analyzing the metabolic status in health and disease.
649 *Nat. Protoc.* 8, 1149–1154 (2013).
- 650 25. Fowler, S.D.; Greenspan, P. Application of Nile red, a fluorescent hydrophobic
651 probe, for the detection of neutral lipid deposits in tissue sections: Comparison
652 with oil red O. *J. Histochem. Cytochem.* 33, 833–836(1985).
- 653 26. Wigglesworth, V.B. Histological staining of lipids for the light and electron
654 microscope. *Biol. Rev. Camb. Philos. Soc.* 63, 417–431(1988).
- 655 27. Cajka, T.; Fiehn, O. Comprehensive analysis of lipids in biological systems by
656 liquid chromatography-mass spectrometry. *TrAC - Trends Anal. Chem.* 61, 192–
657 206(2014).
- 658 28. Long, N.P.; Park, S.; Anh, N.H.; et al. Advances in Liquid Chromatography–Mass
659 Spectrometry-Based Lipidomics: A Look Ahead. *J. Anal. Test.* 4, 183–197(2020).
- 660 29. Berkecz, R.; Tömösi, F.; Körmöczi, T.; Szegedi, V.; Horváth, J.; Janáky, T.
661 Comprehensive phospholipid and sphingomyelin profiling of different brain
662 regions in mouse model of anxiety disorder using online two-dimensional
663 (HILIC/RP)-LC/MS method. *J. Pharm. Biomed. Anal.* 149, 308–317(2018).
- 664 30. Lin, Y.; Gu, H.; Jiang, L.; et al. Cocaine modifies brain lipidome in mice. *Mol.*
665 *Cell. Neurosci.* 85, 29–44(2017).
- 666 31. Zimmerman, T.A.; Monroe, E.B.; Tucker, K.R.; Rubakhin, S.S.; Sweedler, J. V.
667 Imaging of cells and tissues with mass spectrometry. adding chemical information
668 to imaging. *Methods Cell Biol.* 89, 361–390(2008).
- 669 32. Buchberger, A.R.; DeLaney, K.; Johnson, J.; Li, L. Mass spectrometry imaging:
670 a review of emerging advancements and future insights. *Anal. Chem.* 90, 240–
671 265(2018).
- 672 33. Fahy, E.; Subramaniam, S.; Brown, H.A.; et al. A comprehensive classification
673 system for lipids. *J. Lipid Res.* 46, 839–861(2005).

- 674 34. Saito, Y.; Waki, M.; Hameed, S.; Hayasaka, T.; Setou, M. Development of
675 imaging mass spectrometry. *Biol. Pharm. Bull.* 35, 1417–1424(2012).
- 676 35. Caprioli, R.M.; Farmer, T.B.; Gile, J. Molecular Imaging of Biological Samples:
677 Localization of Peptides and Proteins Using MALDI-TOF MS. *Anal. Chem.* 69,
678 4751–4760(1997).
- 679 36. Goto-Inoue, N.; Hayasaka, T.; Zaima, N.; Setou, M. Imaging mass spectrometry
680 for lipidomics. *Biochim. Biophys. Acta - Mol. Cell Biol. Lipids.* 1811, 961–
681 969(2011).
- 682 37. Eriksson, C.; Masaki, N.; Yao, I.; Hayasaka, T.; Setou, M. MALDI imaging mass
683 spectrometry—a mini review of methods and recent developments. *Mass*
684 *Spectrom.* 2, S0022–S0022(2013).
- 685 38. Wiseman, J.M.; Ifa, D.R.; Song, Q.; Cooks, R.G. Tissue imaging at atmospheric
686 pressure using desorption electrospray ionization (DESI) mass spectrometry.
687 *Angew. Chemie Int. Ed.* 45, 7188–7192(2006).
- 688 39. Anderton, C.R.; Gamble, L.J. Secondary ion mass spectrometry imaging of tissues,
689 cells, and microbial systems. *Micros. Today.* 24, 24–31(2016).
- 690 40. Bokhart, M.T.; Muddiman, D.C. Infrared matrix-assisted laser desorption
691 electrospray ionization mass spectrometry imaging analysis of biospecimens.
692 *Analyst.* 141, 5236–5245(2016).
- 693 41. Robichaud, G.; Barry, J.A.; Garrard, K.P.; Muddiman, D.C. Infrared matrix-
694 assisted laser desorption electrospray ionization (IR-MALDESI) imaging source
695 coupled to a FT-ICR mass spectrometer. *J. Am. Soc. Mass Spectrom.* 24, 92–
696 100(2013).
- 697 42. Schaepe, K.; Bhandari, D.R.; Werner, J.; et al. Imaging of lipids in native human
698 bone sections using TOF-secondary ion mass spectrometry, atmospheric pressure
699 scanning microprobe matrix-assisted laser desorption/ionization orbitrap mass
700 spectrometry, and orbitrap-secondary ion mass spectrometry. *Anal. Chem.* 90,
701 8856–8864(2018).
- 702 43. Kompauer, M.; Heiles, S.; Spengler, B. Atmospheric pressure MALDI mass
703 spectrometry imaging of tissues and cells at 1.4- μ m lateral resolution. *Nat.*
704 *Methods.* 14, 90–96(2016).
- 705 44. Tata, A.; Fernandes, A.M.A.P.; Santos, V.G.; Alberici, R.M.; Araldi, D.; Parada,
706 C.A.; Braguini, W.; Veronez, L.; Silva Bisson, G.; Reis, F.H.Z.; et al.
707 Nanoassisted laser desorption-ionization-MS imaging of tumors. *Anal. Chem.*
708 2012, 84, 6341–6345(2012).
- 709 45. Kuwata, K.; Itou, K.; Kotani, M.; Ohmura, T.; Naito, Y. DIUTHAME enables
710 matrix - free mass spectrometry imaging of frozen tissue sections. *Rapid*
711 *Commun. Mass Spectrom.* 34(2020).
- 712 46. Nemes, P.; Woods, A.S.; Vertes, A. Simultaneous imaging of small metabolites
713 and lipids in rat brain tissues at atmospheric pressure by laser ablation electrospray
714 ionization mass spectrometry. *Anal. Chem.* 82, 982–988(2010).
- 715 47. Luo, Z.; He, J.; Chen, Y.; et al. Air flow-assisted ionization imaging mass
716 spectrometry method for easy whole-body molecular imaging under ambient
717 conditions. *Anal. Chem.* 85, 2977–2982(2013).
- 718 48. Alberici, R.M.; Vendramini, P.H.; Eberlin, M.N. Easy ambient sonic-spray
719 ionization mass spectrometry for tissue imaging. *Anal. Methods.* 9, 5029–
720 5036(2017).

- 721 49. Sugiura, Y.; Shimma, S.; Setou, M. Thin sectioning improves the peak intensity
722 and signal-to-noise ratio in direct tissue mass spectrometry. *J. Mass Spectrom.*
723 *Soc. Jpn.* 54, 45–48(2006).
- 724 50. Leopold, J.; Popkova, Y.; Engel, K.M.; Schiller, J. Recent developments of useful
725 MALDI matrices for the mass spectrometric characterization of lipids.
726 *Biomolecules.* 8(2018).
- 727 51. Wang, H.Y.J.; Post, S.N.J.J.; Woods, A.S. A minimalist approach to MALDI
728 imaging of glycerophospholipids and sphingolipids in rat brain sections. *Int. J.*
729 *Mass Spectrom.* 278, 143–149(2008).
- 730 52. Vermillion-Salsbury, R.L.; Hercules, D.M. 9-Aminoacridine as a matrix for
731 negative mode matrix-assisted laser desorption/ionization. *Rapid Commun. Mass*
732 *Spectrom.* 16, 1575–1581(2002).
- 733 53. Hayasaka, T.; Goto-Inoue, N.; Masaki, N.; Ikegami, K.; Setou, M. Application of
734 2,5-dihydroxyacetophenone with sublimation provides efficient ionization of
735 lipid species by atmospheric pressure matrix-assisted laser desorption/ionization
736 imaging mass spectrometry. *Surf. Interface Anal.* **2014**, 46, 1219–1222(2014).
- 737 54. Wang, Z.; Cai, Y.; Wang, Y.; Zhou, X.; Zhang, Y.; Lu, H. Improved MALDI
738 imaging MS analysis of phospholipids using graphene oxide as new matrix. *Sci.*
739 *Rep.* 7, 1–9(2017).
- 740 55. Ibrahim, H.; Jurcic, K.; Wang, J.S.H.; Whitehead, S.N.; Yeung, K.K.C. 1,6-
741 Diphenyl-1,3,5-hexatriene (DPH) as a novel matrix for maldi ms imaging of fatty
742 acids, phospholipids, and sulfatides in brain tissues. *Anal. Chem.* 89, 12828–
743 12836(2017).
- 744 56. Shimma, S.; Sugiura, Y. Effective sample preparations in imaging mass
745 spectrometry. *Mass Spectrom.* 3, S0029–S0029(2014).
- 746 57. Passarelli, M.K.; Winograd, N. Lipid imaging with time-of-flight secondary ion
747 mass spectrometry (ToF-SIMS). *Biochim. Biophys. Acta - Mol. Cell Biol. Lipids,*
748 1811, 976–990(2011).
- 749 58. Li, H.W.; Hua, X.; Long, Y.T. Metal/matrix enhanced time-of-flight secondary
750 ion mass spectrometry for single cell lipids analysis. *Chinese J. Anal. Chem.* 46,
751 61–66(2018).
- 752 59. Malm, J.; Giannaras, D.; Riehle, M.O.; Gadegaard, N.; Sjövall, P. Fixation and
753 drying protocols for the preparation of cell samples for time-of-flight secondary
754 ion mass spectrometry analysis. *Anal. Chem.* 81, 7197–7205(2009).
- 755 60. *Imaging Mass Spectrometry*; Setou, M., Ed.; Springer Japan: Tokyo, ISBN 978-
756 4-431-09424-1(2010).
- 757 61. Dreisewerd, K. The desorption process in MALDI. *Chem. Rev.* 103, 395–
758 425(2003).
- 759 62. Murray, K.K. Lasers for matrix - assisted laser desorption ionization. *J. Mass*
760 *Spectrom.* (2020).
- 761 63. Takats, Z.; Wiseman, J.M.; Gologan, B.; Cooks, R.G. Mass spectrometry
762 sampling under ambient conditions with desorption electrospray ionization.
763 *Science.* 306, 471–473(2004).
- 764 64. Yin, R.; Burnum-Johnson, K.E.; Sun, X.; Dey, S.K.; Laskin, J. High spatial
765 resolution imaging of biological tissues using nanospray desorption electrospray
766 ionization mass spectrometry. *Nat. Protoc.* 14, 3445–3470(2019).

- 767 65. Nguyen, S.N.; Sontag, R.L.; Carson, J.P.; Corley, R.A.; Ansong, C.; Laskin, J.
768 Towards high-resolution tissue imaging using nanospray desorption electrospray
769 ionization mass spectrometry coupled to shear force microscopy. *J. Am. Soc.*
770 *Mass Spectrom.* 29, 316–322(2018).
- 771 66. Yin, R.; Kyle, J.; Burnum-Johnson, K.; Bloodsworth, K.J.; Sussel, L.; Ansong,
772 C.; Laskin, J. High spatial resolution imaging of mouse pancreatic islets using
773 nanospray desorption electrospray ionization mass spectrometry. *Anal. Chem.* 90,
774 6548–6555(2018).
- 775 67. Parrot, D.; Papazian, S.; Foil, D.; Tasdemir, D. Imaging the unimaginable:
776 desorption electrospray ionization – imaging mass spectrometry (DESI-IMS) in
777 natural product research. *Planta Med.* 84, 584–593(2018).
- 778 68. Eberlin, L.S.; Ferreira, C.R.; Dill, A.L.; Ifa, D.R.; Cooks, R.G. Desorption
779 electrospray ionization mass spectrometry for lipid characterization and biological
780 tissue imaging. *Biochim. Biophys. Acta - Mol. Cell Biol. Lipids.* 1811, 946–
781 960(2011).
- 782 69. Chandra, S. Challenges of biological sample preparation for SIMS imaging of
783 elements and molecules at subcellular resolution. *Appl. Surf. Sci.* 255, 1273–
784 1284(2008).
- 785 70. Wishart, D.S.; Tzur, D.; Knox, C.; et al. HMDB: The human metabolome database.
786 *Nucleic Acids Res.* 35(2007).
- 787 71. Mullard, A. Finding the way with LIPID MAPS. *Nat. Rev. Mol. Cell Biol.* 9, 92–
788 92(2008).
- 789 72. Islam, A.; Takeyama, E.; Mamun, M. Al; et al. Green nut oil or DHA
790 supplementation restored decreased distribution levels of DHA containing
791 phosphatidylcholines in the brain of a mouse model of dementia. *Metabolites.*
792 10(2020).
- 793 73. Ide, Y.; Waki, M.; Hayasaka, T.; et al. Human breast cancer tissues contain
794 abundant phosphatidylcholine(36:1) with high stearoyl-coa desaturase-1
795 expression. *PLoS One.* 8, e61204(2013).
- 796 74. Uehara, T.; Kikuchi, H.; Miyazaki, S.; et al. Overexpression of
797 lysophosphatidylcholine acyltransferase 1 and concomitant lipid alterations in
798 gastric cancer. *Ann. Surg. Oncol.* 23, 206–213(2016).
- 799 75. Sparvero, L.J.; Amoscato, A.A.; Dixon, C.E.; et al. Mapping of phospholipids by
800 MALDI imaging (MALDI-MSI): Realities and expectations. *Chem. Phys. Lipids.*
801 165, 545–562(2012).
- 802 76. Sugiura, Y.; Konishi, Y.; Zaima, N.; et al. Visualization of the cell-selective
803 distribution of PUFA-containing phosphatidylcholines in mouse brain by imaging
804 mass spectrometry. *J. Lipid Res.* 50, 1776–1788(2009).
- 805 77. Kobayashi, Y.; Hayasaka, T.; Setou, M.; Itoh, H.; Kanayama, N. Comparison of
806 phospholipid molecular species between terminal and stem villi of human term
807 placenta by imaging mass spectrometry. *Placenta.* 31, 245–248(2010).
- 808 78. Kurabe, N.; Igarashi, H.; Ohnishi, I.; et al. Visualization of sphingolipids and
809 phospholipids in the fundic gland mucosa of human stomach using imaging mass
810 spectrometry. *World J. Gastrointest. Pathophysiol.* 7, 235(2016).
- 811 79. Ellis, S.R.; Wu, C.; Deeley, J.M.; et al. Imaging of human lens lipids by desorption
812 electrospray ionization mass spectrometry. *J. Am. Soc. Mass Spectrom.* 21, 2095–
813 2104(2010).

- 814 80. Carter, C.L.; McLeod, C.W.; Bunch, J. Imaging of phospholipids in formalin
815 fixed rat brain sections by matrix assisted laser desorption/ionization mass
816 spectrometry. *J. Am. Soc. Mass Spectrom.* 22, 1991–1998(2011).
- 817 81. Jackson, S.N.; Ugarov, M.; Egan, T.; et al. MALDI-ion mobility-TOFMS imaging
818 of lipids in rat brain tissue. *J. Mass Spectrom.* 42, 1093–1098(2007).
- 819 82. Cerruti, C.D.; Benabdellah, F.; Lapr evote, O.; Touboul, D.; Brunelle, A. MALDI
820 imaging and structural analysis of rat brain lipid negative ions with 9-
821 aminoacridine matrix. *Anal. Chem.* 84, 2164–2171(2012).
- 822 83. Jackson, S.N.; Baldwin, K.; Muller, L.; et al. Imaging of lipids in rat heart by
823 MALDI-MS with silver nanoparticles. *Anal. Bioanal. Chem.* 406, 1377–
824 1386(2014).
- 825 84. Flinders, B.; Huizing, L.R.S.; Van Heerden, M.; et al. Cross-Species Molecular
826 Imaging of Bile Salts and Lipids in Liver: Identification of Molecular Structural
827 Markers in Health and Disease. *Anal. Chem.* 90, 11835–11846(2018).
- 828 85. Murphy, R.C.; Hankin, J.A.; Barkley, R.M. Imaging of lipid species by MALDI
829 mass spectrometry. (2009).
- 830 86. Berry, K.A.Z.; Li, B.; Reynolds, S.D.; et al. MALDI imaging MS of phospholipids
831 in the mouse lung. *J. Lipid Res.* 52, 1551–1560(2011).
- 832 87. Seng, J.; Nealon, J.; Blanksby, S.; Mitchell, T. Distribution of
833 glycerophospholipids in the adult human lens. *Biomolecules.* 8, 156(2018).
- 834 88. Sj ovall, P.; Lausmaa, J.; Johansson, B. Mass spectrometric imaging of lipids in
835 brain tissue. *Anal. Chem.* 76, 4271–4278(2004).
- 836 89. Touboul, D.; Brunelle, A. TOF-SIMS imaging of lipids on rat brain sections.
837 *Methods Mol. Biol.* 1203, 21–27(2015).
- 838 90. Magnusson, Y.; Friberg, P.; Sj ovall, P.; Dangardt, F.; Malmberg, P.; Chen, Y.
839 Lipid imaging of human skeletal muscle using TOF-SIMS with bismuth cluster
840 ion as a primary ion source. *Clin. Physiol. Funct. Imaging.* 28, 202–209(2008).
- 841 91. Hameed, S.; Ikegami, K.; Sugiyama, E.; et al. Direct profiling of the phospholipid
842 composition of adult *Caenorhabditis elegans* using whole-body imaging mass
843 spectrometry. *Anal. Bioanal. Chem.* 407, 7589–7602(2015).
- 844 92. Niehoff, A.C.; Kettling, H.; Pirkl, A.; Chiang, Y.N.; Dreisewerd, K.; Yew, J.Y.
845 Analysis of drosophila lipids by matrix-assisted laser desorption/ionization mass
846 spectrometric imaging. *Anal. Chem.* 86, 11086–11092(2014).
- 847 93. Sans, M.; Gharpure, K.; Tibshirani, R.; et al. Metabolic markers and statistical
848 prediction of serous ovarian cancer aggressiveness by ambient ionization mass
849 spectrometry imaging. *Cancer Res.* 77, 2903–2913(2017).
- 850 94. Masterson, T.A.; Dill, A.L.; Eberlin, L.S.; et al. Distinctive glycerophospholipid
851 profiles of human seminoma and adjacent normal tissues by desorption
852 electrospray ionization imaging mass spectrometry. *J. Am. Soc. Mass Spectrom.*
853 22, 1326–1333(2011).
- 854 95. Margulis, K.; Chiou, A.S.; Aasi, S.Z.; Tibshirani, R.J.; Tang, J.Y.; Zare, R.N.
855 Distinguishing malignant from benign microscopic skin lesions using desorption
856 electrospray ionization mass spectrometry imaging. *Proc. Natl. Acad. Sci. U. S.*
857 *A.* 115, 6347–6352(2018).
- 858 96. Morita, Y.; Sakaguchi, T.; Ikegami, K.; et al. Lysophosphatidylcholine
859 acyltransferase 1 altered phospholipid composition and regulated hepatoma
860 progression. *J. Hepatol.* 59, 292–299(2013).

- 861 97. Ikedo, T.; Minami, M.; Kataoka, H.; et al. Imaging mass spectroscopy delineates
862 the thinned and thickened walls of intracranial aneurysms. *Biochem. Biophys. Res.*
863 *Commun.* 495, 332–338(2018).
- 864 98. Koizumi, S.; Yamamoto, S.; Hayasaka, T.; et al. Imaging mass spectrometry
865 revealed the production of lyso-phosphatidylcholine in the injured ischemic rat
866 brain. *Neuroscience.* 168, 219–225(2010).
- 867 99. Mihara, Y.; Horikawa, M.; Sato, S.; et al. Lysophosphatidic acid precursor levels
868 decrease and an arachidonic acid-containing phosphatidylcholine level increases
869 in the dorsal root ganglion of mice after peripheral nerve injury. *Neurosci. Lett.*
870 698, 69–75(2019).
- 871 100. Aoki, J.; Taira, A.; Takanezawa, Y.; et al. Serum lysophosphatidic acid is
872 produced through diverse phospholipase pathways. *J. Biol. Chem.* 277, 48737–
873 48744(2002).
- 874 101. Yuki, D.; Sugiura, Y.; Zaima, N.; et al. DHA-PC and PSD-95 decrease
875 after loss of synaptophysin and before neuronal loss in patients with Alzheimer’s
876 disease. *Sci. Rep.* 4(2014).
- 877 102. Takeyama, E.; Islam, A.; Watanabe, N.; et al. Dietary intake of green nut
878 oil or DHA ameliorates DHA distribution in the brain of a mouse model of
879 dementia accompanied by memory recovery. *Nutrients.* 11(2019).
- 880 103. Philipsen, M.H.; Phan, N.T.N.; Fletcher, J.S.; Malmberg, P.; Ewing, A.G.
881 Mass spectrometry imaging shows cocaine and methylphenidate have opposite
882 effects on major lipids in drosophila brain. *ACS Chem. Neurosci.* 9, 1462–
883 1468(2018).
- 884 104. Kurabe, N.; Hayasaka, T.; Ogawa, M.; et al. Accumulated
885 phosphatidylcholine (16:0/16:1) in human colorectal cancer; possible
886 involvement of LPCAT4. *Cancer Sci.* 104, 1295–1302(2013).
- 887 105. Hosokawa, Y.; Masaki, N.; Takei, S.; et al. Recurrent triple-negative
888 breast cancer (TNBC) tissues contain a higher amount of phosphatidylcholine
889 (32:1) than non-recurrent TNBC tissues. *PLoS One.* 12, e0183724(2017).
- 890 106. Goto, T.; Terada, N.; Inoue, T.; et al. Decreased expression of
891 lysophosphatidylcholine (16:0/OH) in high resolution imaging mass spectrometry
892 independently predicts biochemical recurrence after surgical treatment for
893 prostate cancer. *Prostate.* 75, 1821–1830(2015).
- 894 107. Dill, A.L.; Eberlin, L.S.; Costa, A.B.; et al. Multivariate statistical
895 identification of human bladder carcinomas using ambient ionization imaging
896 mass spectrometry. *Chem. - A Eur. J.* 17, 2897–2902(2011).
- 897 108. Eberlin, L.S.; Norton, I.; Dill, A.L.; et al. Classifying human brain tumors
898 by lipid imaging with mass spectrometry. *Cancer Res.* 72, 645–654(2012).
- 899 109. Dill, A.L.; Eberlin, L.S.; Zheng, C.; et al. Multivariate statistical
900 differentiation of renal cell carcinomas based on lipidomic analysis by ambient
901 ionization imaging mass spectrometry. *Anal. Bioanal. Chem.* 398, 2969–
902 2978(2010).
- 903 110. Guenther, S.; Muirhead, L.J.; Speller, A.V.M.; et al. Spatially resolved
904 metabolic phenotyping of breast cancer by desorption electrospray ionization
905 mass spectrometry. *Cancer Res.* 75, 1828–1837(2015).
- 906 111. Mao, X.; He, J.; Li, T.; et al. Application of imaging mass spectrometry
907 for the molecular diagnosis of human breast tumors. *Sci. Rep.* 6, 1–12(2016).

- 908 112. Stubbs, C.D.; Smith, A.D. The modification of mammalian membrane
909 polyunsaturated fatty acid composition in relation to membrane fluidity and
910 function. *BBA - Rev. Biomembr.* 779, 89–137(1984).
- 911 113. Ishikawa, S.; Tateya, I.; Hayasaka, T.; et al. The distribution of
912 phosphatidylcholine species in superficial-type pharyngeal carcinoma. *Biomed*
913 *Res. Int.* (2017).
- 914 114. Kiebish, M.A.; Han, X.; Cheng, H.; Chuang, J.H.; Seyfried, T.N.
915 Cardiolipin and electron transport chain abnormalities in mouse brain tumor
916 mitochondria: Lipidomic evidence supporting the Warburg theory of cancer. *J.*
917 *Lipid Res.* 49, 2545–2556(2008).
- 918 115. Hayasaka, T.; Fuda, H.; Hui, S.-P.; Chiba, H. Imaging mass spectrometry
919 reveals a decrease of cardiolipin in the kidney of NASH model mice. *Anal. Sci.*
920 32, 473–476(2016).
- 921 116. Amoscato, A.A.; Sparvero, L.J.; He, R.R.; Watkins, S.; Bayir, H.; Kagan,
922 V.E. Imaging mass spectrometry of diversified cardiolipin molecular species in
923 the brain. *Anal. Chem.* 86, 6587–6595(2014).
- 924 117. Sparvero, L.J.; Amoscato, A.A.; Fink, A.B.; et al. Imaging mass
925 spectrometry reveals loss of polyunsaturated cardiolipins in the cortical contusion,
926 hippocampus, and thalamus after traumatic brain injury. *J. Neurochem.* 139, 659–
927 675(2016).
- 928 118. Yang, H.; Jackson, S.N.; Woods, A.S.; Goodlett, D.R.; Ernst, R.K.; Scott,
929 A.J. Streamlined analysis of cardiolipins in prokaryotic and eukaryotic samples
930 using a norharmane matrix by MALDI-MSI. *J. Am. Soc. Mass Spectrom.* 31,
931 2495–2502(2020).
- 932 119. Eberlin, L.S.; Gabay, M.; Fan, A.C.; et al. Alteration of the lipid profile in
933 lymphomas induced by MYC overexpression. *Proc. Natl. Acad. Sci. U. S. A.* 111,
934 10450–10455(2014).
- 935 120. Zhang, J.; Yu, W.; Ryu, S.W.; et al. Cardiolipins are biomarkers of
936 mitochondria-rich thyroid oncocytic tumors. *Cancer Res.* 76, 6588–6597(2016).
- 937 121. Spickett, C.M.; Pitt, A.R. Oxidative lipidomics coming of age: Advances
938 in analysis of oxidized phospholipids in physiology and pathology. *Antioxidants*
939 *Redox Signal.* 22, 1646–1666(2015).
- 940 122. Li, L.; Zhong, S.; Shen, X.; et al. Recent development on liquid
941 chromatography-mass spectrometry analysis of oxidized lipids. *Free Radic. Biol.*
942 *Med.* 144, 16–34(2019).
- 943 123. Hossen, M.A.; Nagata, Y.; Waki, M.; et al. Decreased level of
944 phosphatidylcholine (16:0/20:4) in multiple myeloma cells compared to plasma
945 cells: a single-cell MALDI-IMS approach. *Anal. Bioanal. Chem.* 407, 5273–
946 5280(2015).
- 947 124. Schober, Y.; Guenther, S.; Spengler, B.; Römpf, A. Single cell matrix-
948 assisted laser desorption/ionization mass spectrometry imaging. *Anal. Chem.* 84,
949 6293–6297(2012).
- 950 125. Ostrowski, S.G.; Van Bell, C.T.; Winograd, N.; Ewing, A.G. Mass
951 spectrometric imaging of highly curved membranes during *Tetrahymena* mating.
952 *Science.* 305, 71–73(2004).

- 953 126. Patterson, N.H.; Doonan, R.J.; Daskalopoulou, S.S.; et al. Three-
954 dimensional imaging MS of lipids in atherosclerotic plaques: Open-source
955 methods for reconstruction and analysis. *Proteomics*. 16, 1642–1651(2016).
- 956 127. Dueñas, M.E.; Essner, J.J.; Lee, Y.J. 3D MALDI mass spectrometry
957 imaging of a single cell: spatial mapping of lipids in the embryonic development
958 of Zebrafish. *Sci. Rep.* 7(2017).
- 959 128. Paine, M.R.L.; Liu, J.; Huang, D.; et al. Three-dimensional mass
960 spectrometry imaging identifies lipid markers of medulloblastoma metastasis. *Sci.*
961 *Rep.* 9(2019).
- 962 129. Eberlin, L.S.; Ifa, D.R.; Wu, C.; Cooks, R.G. Three-dimensional
963 visualization of mouse brain by lipid analysis using ambient ionization mass
964 spectrometry. *Angew. Chemie*. 122, 885–888(2010).
- 965 130. Henderson, F.; Jones, E.; Denbigh, J.; et al. 3D DESI-MS lipid imaging in
966 a xenograft model of glioblastoma: a proof of principle. *Sci. Rep.* 10(2020).
- 967 131. Castellanos, A.; Ramirez, C.E.; Michalkova, V.; Nouzova, M.; Noriega,
968 F.G.; Fernández-Lima, F. Three dimensional secondary ion mass spectrometry
969 imaging (3D-SIMS) of: *Aedes aegypti* ovarian follicles. *J. Anal. At. Spectrom.* 34,
970 874–883(2019).
- 971 132. Angel, P.M.; Baldwin, H.S.; Gottlieb Sen, D.; et al. Advances in MALDI
972 imaging mass spectrometry of proteins in cardiac tissue, including the heart valve.
973 *Biochim. Biophys. Acta - Proteins Proteomics*. 1865, 927–935(2017).
- 974 133. Nakashima, Y.; Setou, M. Distribution of antisense oligonucleotides in rat
975 eyeballs using maldi imaging mass spectrometry. *Mass Spectrom.* 7, A0070–
976 A0070(2018).
- 977 134. Eto, F.; Sato, S.; Setou, M.; Yao, I. Region-specific effects of Scrapper on
978 the abundance of glutamate and gamma-aminobutyric acid in the mouse brain. *Sci.*
979 *Rep.* 10, 1–10(2020).
- 980 135. Shrivastava, K.; Hayasaka, T.; Sugiura, Y.; Setou, M. Method for
981 simultaneous imaging of endogenous low molecular weight metabolites in mouse
982 brain using TiO₂ nanoparticles in nanoparticle-assisted laser
983 desorption/ionization-imaging mass spectrometry. *Anal. Chem.* 83, 7283–
984 7289(2011).
- 985 136. Sugiura, Y.; Setou, M. Imaging mass spectrometry for visualization of
986 drug and endogenous metabolite distribution: Toward in situ
987 pharmacometabolomes. *J. Neuroimmune Pharmacol.* 5, 31–43(2010).
- 988 137. Sugiura, Y.; Shimma, S.; Setou, M. Two-step matrix application technique
989 to improve ionization efficiency for matrix-assisted laser desorption/ionization in
990 imaging mass spectrometry. *Anal. Chem.* 78, 8227–8235(2006).
- 991 138. Taira, S.; Sugiura, Y.; Moritake, S.; Shimma, S.; Ichiyanagi, Y.; Setou, M.
992 Nanoparticle-assisted laser desorption/ionization based mass imaging with
993 cellular resolution. *Anal. Chem.* 80, 4761–4766(2008).
- 994 139. Mamun, M. Al; Sato, S.; Naru, E.; et al. Higher Accumulation of
995 Docosahexaenoic Acid in the Vermilion of the Human Lip than in the Skin. *Int.*
996 *J. Mol. Sci.* 21, 2807(2020).
- 997 140. Mamun, M. Al; Gonzalez, T.V.; Islam, A.; et al. Analysis of potential anti-
998 aging beverage Pru, a traditional Cuban refreshment, by desorption electrospray

999 ionization-mass spectrometry and FTICR tandem mass spectrometry. *J. Food*
1000 *Drug Anal.* 27(4), 833-840(2019).

1001 141. Sato, T.; Horikawa, M.; Takei, S.; et al. Preferential incorporation of
1002 administered eicosapentaenoic acid into thin-cap atherosclerotic plaques.
1003 *Arterioscler. Thromb. Vasc. Biol.* 39, 1802–1816(2019).

1004